Electronic Supplementary Information (ESI) for

Insights into the defect-driven heterogeneous structural evolution of Ni-rich layered cathode in lithium-ion batteries

Zhongyuan Huang,[a] Ziwei Chen,[a] Maolin Yang,[a] Mihai Chu,[b] Zenan Li,[c] Sihao Deng,[de] Lunhua He,[efg] Lei Jin,[h] Rafal E. Dunin-Borkowski,[h] Rui Wang,*[i] Jun Wang,*[c] Tingting Yang,* [ah] and Yinguo Xiao*[a]

[a] School of Advanced Materials, Peking University, Shenzhen Graduate School, Shenzhen 518055, PR China

[b] Department of Chemistry, Materials, and Chemical Engineering "Giulio Natta", Politecnico di Milano, Milano 20133, Italy

[c] School of Innovation and Entrepreneurship, Southern University of Science and Technology, Shenzhen 518055, PR China

[d] Institute of High Energy Physics, Chinese Academy of Sciences, Beijing 100049, PR China

[e] Spallation Neutron Source Science Center, Dongguan 523803, PR China

[f] Beijing National Laboratory for Condensed Matter Physics, Institute of Physics, Chinese Academy of Sciences, Beijing 100190, PR China

[g] Songshan Lake Materials Laboratory, Dongguan 523808, PR China

[h] Ernst Ruska-Centre for Microscopy and Spectroscopy with Electrons, Forschungszentrum Jülich GmbH, Jülich 52428, Germany

[i] Department of Engineering, University of Cambridge, Cambridge CB30FS, UK

* Corresponding Authors: Rui Wang (rw716@cam.ac.uk), Jun Wang (wangj9@sustech.edu.cn), Tingting Yang (t.yang@fz-juelich.de), Yinguo Xiao (y.xiao@pku.edu.cn)

Experimental

Electrode preparations

Layered NCM811 cathode powder was prepared via a solid-state reaction of $Ni_{0.8}Co_{0.1}Mn_{0.1}(OH)_2$ precursor and $LiOH \cdot H_2O$. Detail process was reported in the previous work.[1] Next, the powder product was dispersed in N-methyl-2-pyrrolidone (NMP) with Super P conductive agent and polyvinylidene difluoride (PVDF) at the ratio of 96:2:2 in mass to make the slurry. The slurry was cast onto aluminum foil with the thicknesses of 15 μm, and dried at 110°C for 12 h under vacuum to prepare NCM811 cathode. The active material loading of cathode is 33.8 mg/cm^2. The compacted density of cathode is 3.40 g/cm^3.

Silicon-based composite was prepared by a magnesio-mechanochemical reaction of diatomite and Mg powder. After the reaction, Mg-containing byproducts were removed by HCl etching. The obtained product was then coated with carbon. Details could be found in the previous works.[2,3] Finally, the material consisted of mixed silicon and silica nanodomains and carbon shells, with the mass ratio of near 1:1:1. Two types of anodes were prepared. The first is pure graphite, and the latter is graphite-silicon-silica (GSO) powder with about 95% graphite (from Kejing, Shenzhen, China) and about 5% as-prepared carbon-coated silicon-based composite in mass. The anode powder, Super P, carboxymethyl cellulose sodium (CMC), and polyacrylic acid (PAA) were stirred in deionized water for 5 h with the 95:1.4:0.6:3 mass ratio, then cast onto copper foil with the thicknesses of 11 μm, and dried under the same condition of the cathode to prepare the pure graphite or GSO anodes. The active material loading of anode is 18.4 mg/cm^2. The compacted density of cathode is 1.60 g/cm^3.

Full cell assembles and electrochemical measurements

Full cells were assembled in an Argon-filled glovebox, all of which used the NCM811 cathode and Celgard 2400 separators. The electrolyte was 1 M $LiPF_6$ dissolved in solvent mainly with ethylene carbonate (EC), ethyl methyl carbonate (EMC), diethyl carbonate (DEC) under 1:1:1 in volume. The injection volume was 2.5 g/Ah, which was minimized to reduce the neutron incoherent scattering of H from organic solvents, which guaranteed the quality of *operando* neutron patterns. Negative/positive electrode capacity ratio (N/P) of cells was controlled around 1.1. Cells had the electrode area of 62.7 × 50.0 mm^2 and the thickness of ~3.63 mm, which contained 16 parallel stacking layers of cathode, anode, and separators to enhance the Bragg scattering signal from electrodes. Two types of cells with different anodes were assembled. One type used the pure graphite anode, named as 811|G. Another chose the GSO anode, named as 811|GSO. A batch of 5 basically identical cells were assembled for each type, which would be used for electrochemical measurements (rate and cycling performance)

and further research including *operando* neutron experiment, 4D-STEM, etc. Two cells of each type were used for galvanostatic discharge-charge tests between 2.7 V and 4.3 V on a NEWARE battery test system. One was measured under different rates (0.1C to 1C, 5 cycles for each). Another was charged and discharged once at 0.1C and then cycled at 0.5C.

Operando neutron diffraction experiments

Operando neutron diffraction experiments were carried on the General Purpose Powder Diffractometer (GPPD)[4] at China Spallation Neutron Source (CSNS), Dongguan, Guangdong, China. GPPD is a versatile time-of-flight (TOF) diffractometer with 3 sets of detector banks, of which centers are located at $2\theta = 30°$, $90°$ and $150°$ respectively. It supports research needs of various materials, as well as special environments for *operando* structure studies of cycling cells. Obviously, counting rate is the most critical requirement of an *operando* experiment since it decides the time resolution of a pattern. The gradual upgrade of CSNS facility and efforts from staff permit high enough flux of GPPD to collect the neutron data within acceptable time. Moreover, to maximize the signal collection, beam size was set as 40 mm in height and 20 mm in width.

Before the experiments, 811|G and 811|GSO cells were hanged on the scattering cavity by a sample holder with insulated clamp fixture. Distance from the upper end of the holder to the cell center was about 80 mm. Wires were wound around the holder, and covered with neutron shielding materials to avoid unnecessary signal. One end of the wire was connected to the cell, while another end was connected to a LANHE CT2001A Battery Testing System. After the installation of equipment and the cell, a series of tests was carried out, including checking the cell state, testing external circuit, collecting a pattern for the cell at the static state, etc., to ensure the smooth progress of following experiments.

Before charging the first cell, a 1-hour trial testing was carried out for data quality evaluation. Based on the test result for the uncharged cell, 20 min was decided for one pattern collection. A time gap of ~3 min was left between neighboring patterns for data saving and starting the next. So, the total data collecting time for one pattern is ~23 min. Cells were charged from OCV to 4.3 V under 0.2C, then discharged to 2.7 V (versus corresponding anodes) with the same rate. Charge time of 811|G and 811|GSO during experiments are 5.04 and 5.15 h, while discharge time are 3.85 and 3.99 h, respectively.

Data processing and Rietveld refinements

SOC of each *operando* neutron pattern is determined as follows: First, the static state before charge was defined as the 0% SOC, and the time when the 1st charge was finished was

defined as the 100% SOC. Then the SOC of a pattern (suppose the ith one, $i = 1, 2, 3 \ldots$) during charging could be determined by:

$$SOC_{i,cha.} = \frac{q_{i,cha.}}{q_{cha.}} = \frac{I_{cha.}t_{i,cha.}}{I_{cha.}t_{cha.}} = \frac{t_{i,cha.}}{t_{cha.}}. \tag{S1}$$

In the definition, $q_{i, cha.}$ is the accumulated charge capacity at the mid-time point when the ith pattern was collecting. $q_{cha.}$ is the total charge capacity. $I_{cha.}$ is the charge current. $t_{i, cha.}$ and $t_{cha.}$ are the mid-time point of the ith pattern collection and the total charge time, respectively. Similarly, SOC of patterns during discharging could also be defined by:

$$SOC_{i,dis.} = 1 - \frac{q_{i,dis.}}{q_{cha.}} = 1 - \frac{I_{dis.}t_{i,dis.}}{I_{cha.}t_{cha.}} = 1 - \frac{t_{i,dis.}}{t_{cha.}}. \tag{S2}$$

Since the discharge current $I_{dis.}$ is equal to the charge current, which is 0.2C, the capacity ratio is also converted to the time ratio. It is worthing noting that the total charge capacity is still used as the reference of 100% SOC in this work, rather than the total discharge capacity. The reason is that the crystal structure of electrodes at the end of 1st discharge is usually different from those at the uncharged state due to a degree of irreversibility. If the total discharge capacity were the denominator, value of SOC for the end state would be almost equal to that for the state before charge (0%), leading to a misunderstanding that the final structure might be almost the same as the initial. To avoid that, the 1st charge capacity is used as the standard to calibrate the SOC for neutron data. Additionally, the last data for each cell, which was acquired at almost the end of discharge and a period of quiescent state, was not be assigned the SOC value because it was under neither charge nor discharge.

d-spacing in Å of each neutron data point was determined by converting TOF in μs by:

$$TOF = Z_0 + Dtt_1 d + Dtt_2 d^2. \tag{S3}$$

In this formula, Z_0 is the constant shift. Dtt_1 is the diffractometer constant calibrated by the standard sample. Dtt_2 is the correction coefficient for sample displacement and absorption-induced shifts. Since cells and holders were not moved during *operando* experiments, Z_0 and Dtt_2 for each cell were determined by refining the patterns collected under the uncharged state. The three parameters were fixed when doing structure refinement for other *operando* patterns.

Rietveld refinements were carried out for the neutron data between 0.75 and 2.6 Å through the FullProf Suite.[5] A set of data points located at the position where no Bragg reflection was observed were selected and connected linearly to fit the background. Background points were allowed for optimization during refinements. A Pseudo-Voigt function convoluted with a back-to-back exponential was adopted to describe the peak profile. Peak profile parameters from the instrument resolution file were used as the initial value, which were further optimized. Both the isotropic size and strain parameters were adjusted to match the FWHM of reflections in

operando patterns during refinements. The Lorentz and polarization factors were accounted by multiplying d^4 and $\sin \theta$. Based on the comparison of the refined *operando* data to that from previous *operando* researches[6] or powder samples,[7] refinement results were not noticeably influenced, suggesting that the model could well match the experiment data.

Steps of refinements were shown below: First, scale factors, lattice parameters, background parameters, profile parameters, etc. were refined and optimized to appropriate value. Next, they were fixed and structure parameters, like *z*-coordinate of O at $6c$ site, occupancy of Li at $3a$ site, Li/Ni disordering amount of cathode, etc., were allowed to vary. The following assumptions were used as constrains:

(1) *Constant and uniform composition (except lithium).* The composition ratio of Ni, Co, and Mn was fixed to 8:1:1. Oxygen loss of cathode during charging in this work was ignored, and the occupancy of O at $6c$ site was fixed as 1.

(2) *Li/Ni disordering induced by site exchange.* Once a Ni ion migrated to a neighboring Li site during cycling, one Li ion should migrate to fill the Ni vacancy, forming a site exchange. Vacancies in TM layers were not permitted.

(3) *Lithium extraction occurring in lithium layers.* During refinements, only the Li occupancy at $3a$ site was allowed to vary.

Correlation of structural parameters, which was reduced by restrictions, including fixing atomic displacement parameters, reducing the variation of refined parameters, and restricting the variation ranges. Last, the obtained results were used as the initial value for the refinement of the next. The same steps would repeat for each data. Parameters of current collectors, which did not evolve during cycling, were not refined from the 2nd pattern. Refined structures of crystallized phases in electrodes were visualized by the VESTA program.[8] Contour plots for the two sets of full cell *operando* neutron diffraction data after background subtractions were realized by MATLAB.

4D-STEM and other electron microscopy characterizations

A ZEISS Supra 55 field-emission scanning electron microscope (SEM) equipped with energy dispersive spectrometer (EDS) was used to observe the morphologies and analyze the elements of NCM811 cathode, pure graphite anode, and GSO anode.

One 811|G cell was charged to 4.3 V and disassembled in the Argon-filled glove box. NCM811 powder from two cells was then carefully scaped from the Al foil and washed by DEC to reduce residual salts. After drying, the obtained powder was sealed and used for electron microscopy characterizations. The atomic HAADF imaging was conducted on a FEl Titan G2 ChemisTEM 80-200 transmission electron microscope operated at 200 kV. The microscope is

equipped with a high-brightness field emission gun and a probe aberration corrector for aberration-corrected STEM. Tomography EDS was conducted on a TFS Spectra 300 (S)TEM operated at 300 kV, and the tilting angle was between -55° to 55°. The microscope is equipped with an ultra-high brightness field emission gun, a probe aberration corrector for aberration-corrected STEM and an image aberration corrector for aberration-corrected TEM. 4D-STEM experiment was conducted on Tescan Tensor microscope. which is the world first precession assisted 4D-STEM microscope and can realize near real-time analysis and processing of 4D-STEM data. The 4D-STEM was performed at a convergence semi-angle of 1.5 mrad, beam current of 200 pA, and probe size of 1.5 nm. The diffraction size is 124.5 mrad. The precession angel is 0.8°. The electron probe was raster-scanned across the selection area using a step size of 3.5 nm and a diffraction pattern recorded at each probe position with a high-performance, hybrid-pixel, direct electron diffraction camera (Dectris Quadro). The camera has 512×512 physical pixels, used for the strain measurements. Additionally, 4-fold (128×128 pixels) pixel binning is utilized for orientation and phase mapping.
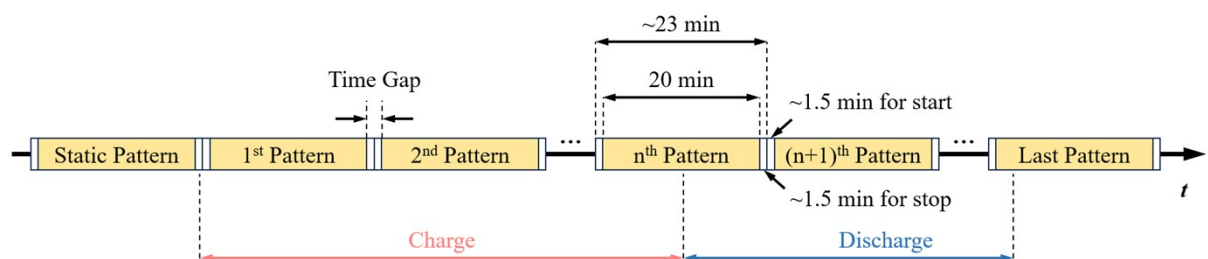
Fig. S1 Schematic of data collection plan and the corresponding electrochemical state of cells during the *operando* neutron experiments.
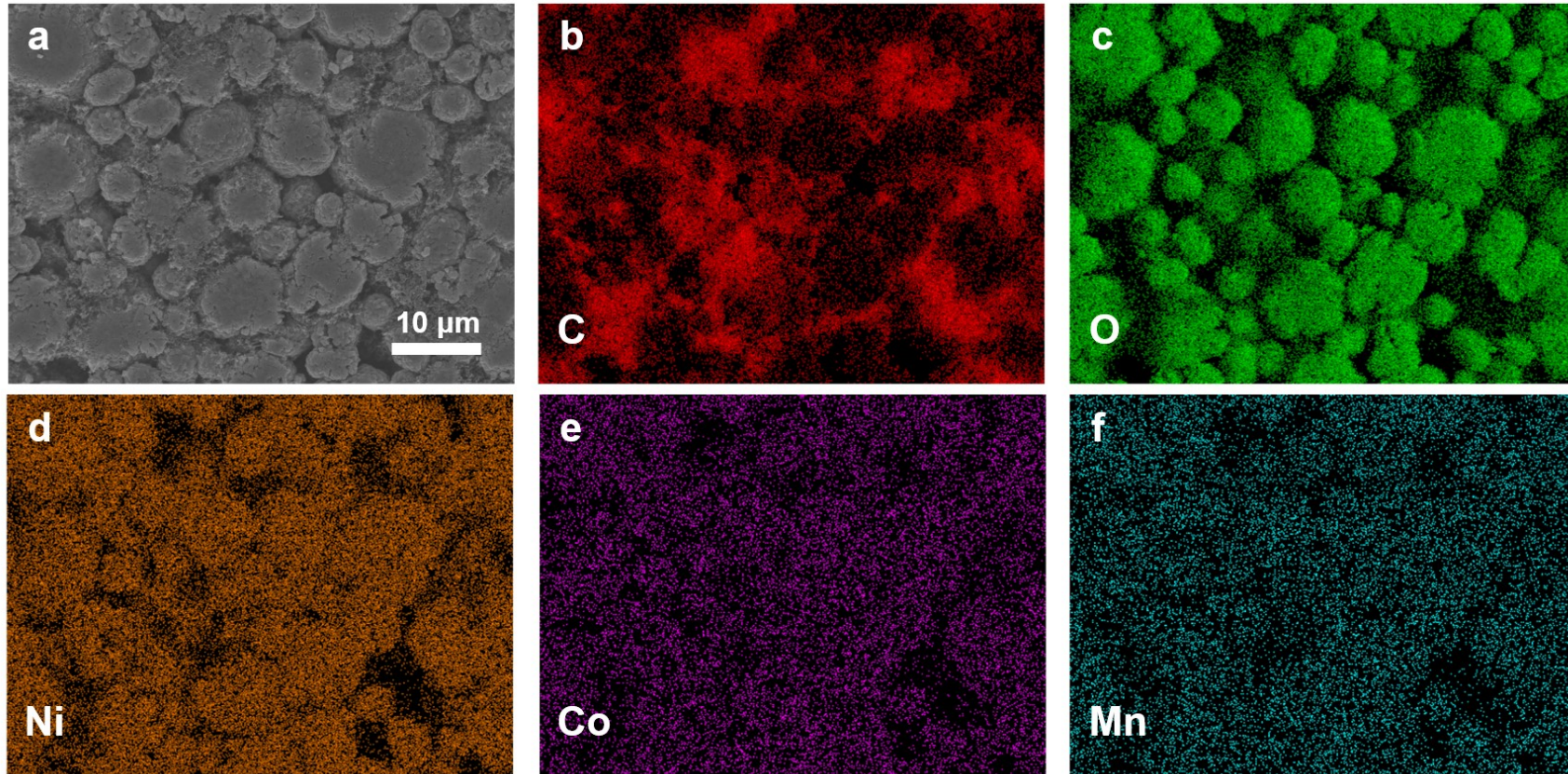
Fig. S2 (a) SEM morphology image of NCM811 cathode and the corresponding EDS mappings of (b) carbon, (c) oxygen, (d) nickel, (e) cobalt, and (f) manganese.
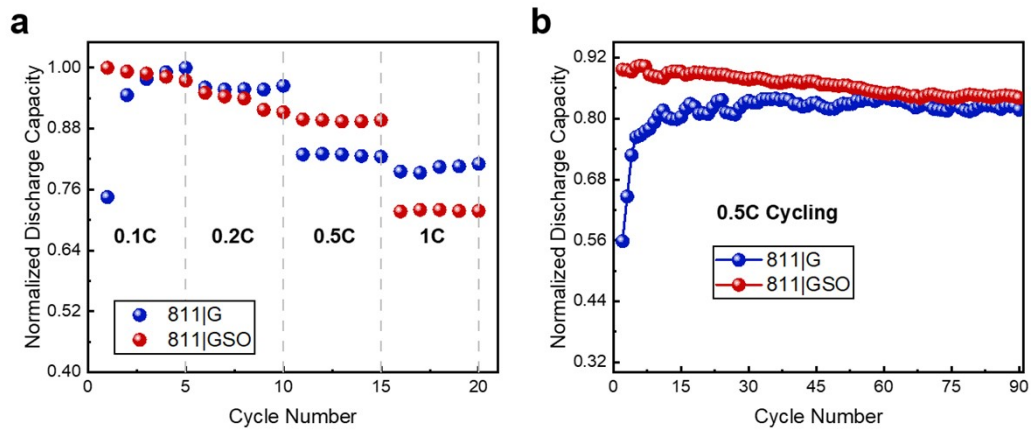
Fig. S3 (a) Rate performance of 811|G and 811|GSO from 0.1C to 1C. (b) Cycling performance of the full cells at 0.5C. Discharge capacity was normalized through dividing by the maximum capacity under 0.1C. Voltage is within the range of 2.7~4.3 V.
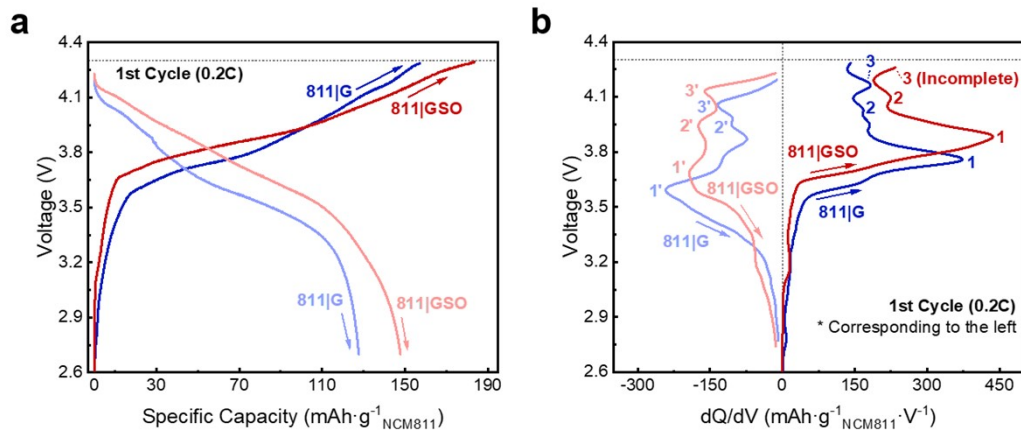
Fig. S4 (a) The 1st 0.2C cycling charge-discharge curve of 811|G and 811|GSO cells between 2.7 and 4.3 V during the *operando* neutron diffraction experiments. (b) Corresponding $dQ \cdot dV^{-1}$ curves of 811|G and 811|GSO cells. Peaks with assigned numbers represent the so-called "phase transitions" reported in previous studies. (1: H1 → M; 2: M → H2; 3: H2 → H3; 1', 2', and 3' are the inverse processes.) Some peaks split due to the inhomogeneous electrochemical delithiation/lithiation during the 1st cycling.
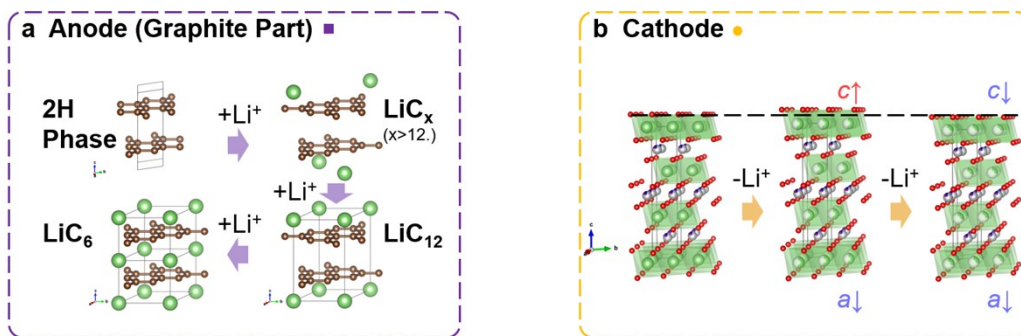
Fig. S5 (a) Schematic of graphite structure transition during lithiation. (b) Schematic of NCM811 structural evolution during delithiation.
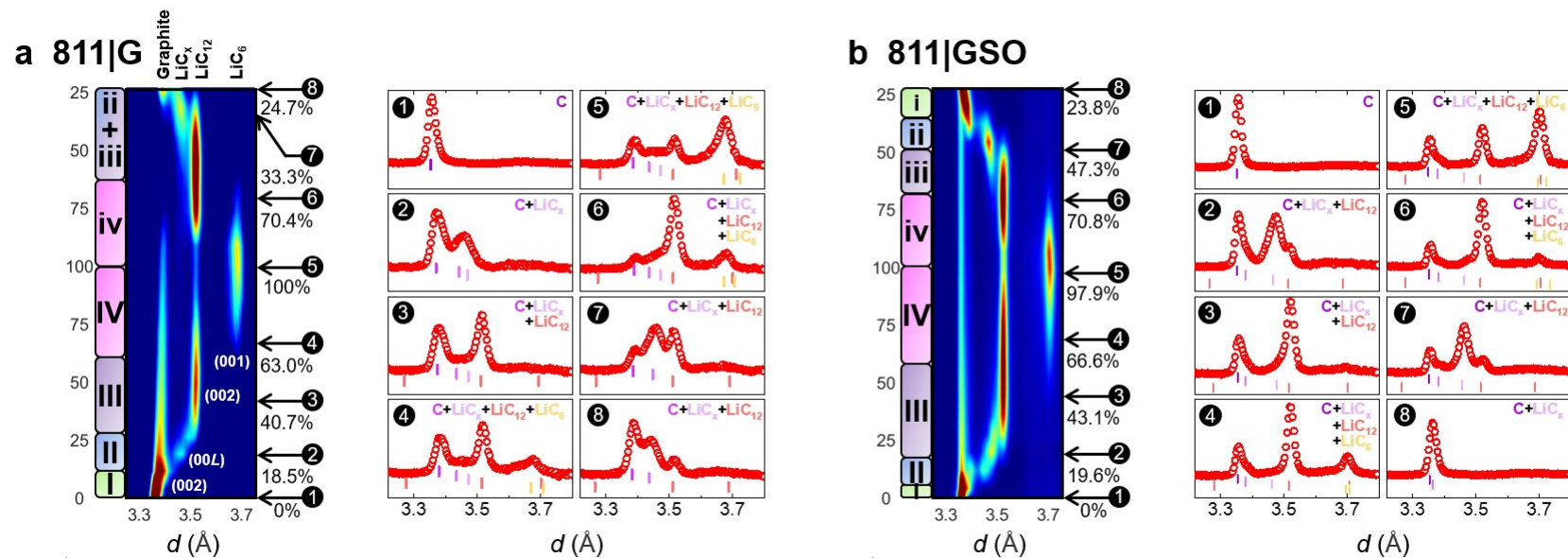
Fig. S6 *Operando* neutron diffraction contour plots and selected patterns at given SOC of (a) 811|G and (b) 811|GSO cells during the 1st 0.2C cycling over the range from 3.25 to 3.75 Å, where only the (00L) reflections of lithiated graphite phases exists. Phases compositions and Miller indices of Bragg reflections are determined and marked on the 811|G contour plot. For each plot, 8 patterns containing phase information are shown on the right, whose SOC could be found through the black circled number markers. Roman numerals on the left of each plot identify main transitions of lithiated graphite during charge/discharge. (I: 2H-graphite → Stage 1L-dilute lithiated graphite; II: Stage 1L-dilute lithiated graphite → Stage 2L/3L/4L-LiC$_x$, x > 12; III: Stage 2L/3L/4L-LiC$_x$, x > 12 → Stage 2-LiC$_{12}$; IV: Stage 2-LiC$_{12}$ → Stage 1-LiC$_6$. Lower-case Roman numerals represent the corresponding reverse transition during discharge.)
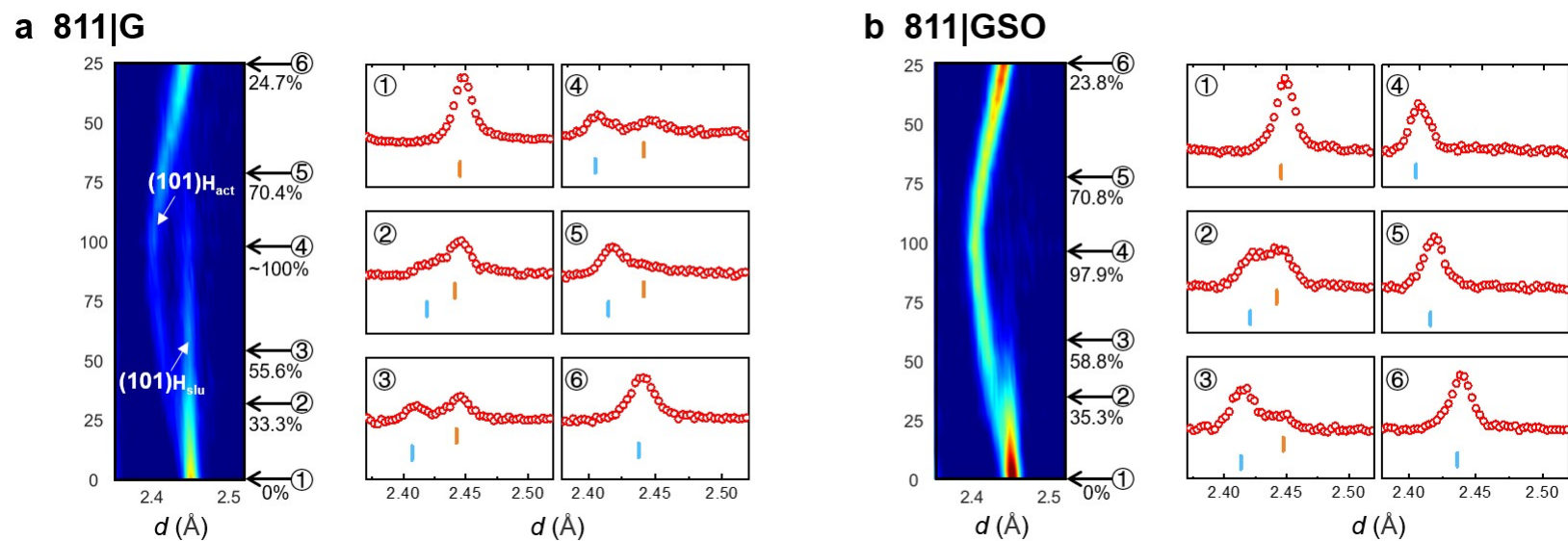
Fig. S7 *Operando* neutron diffraction contour plots and selected patterns at given SOC of (a) 811|G and (b) 811|GSO cells during the 1st 0.2C cycling over the range from 2.35 to 2.52 Å, where splits of NCM811 (101) reflections are observed. The activate and the sluggish parts of the layered cathode are marked on the 811|G contour plot. For each plot, 6 patterns are shown on the right, whose SOC could be found through the white circled number markers.
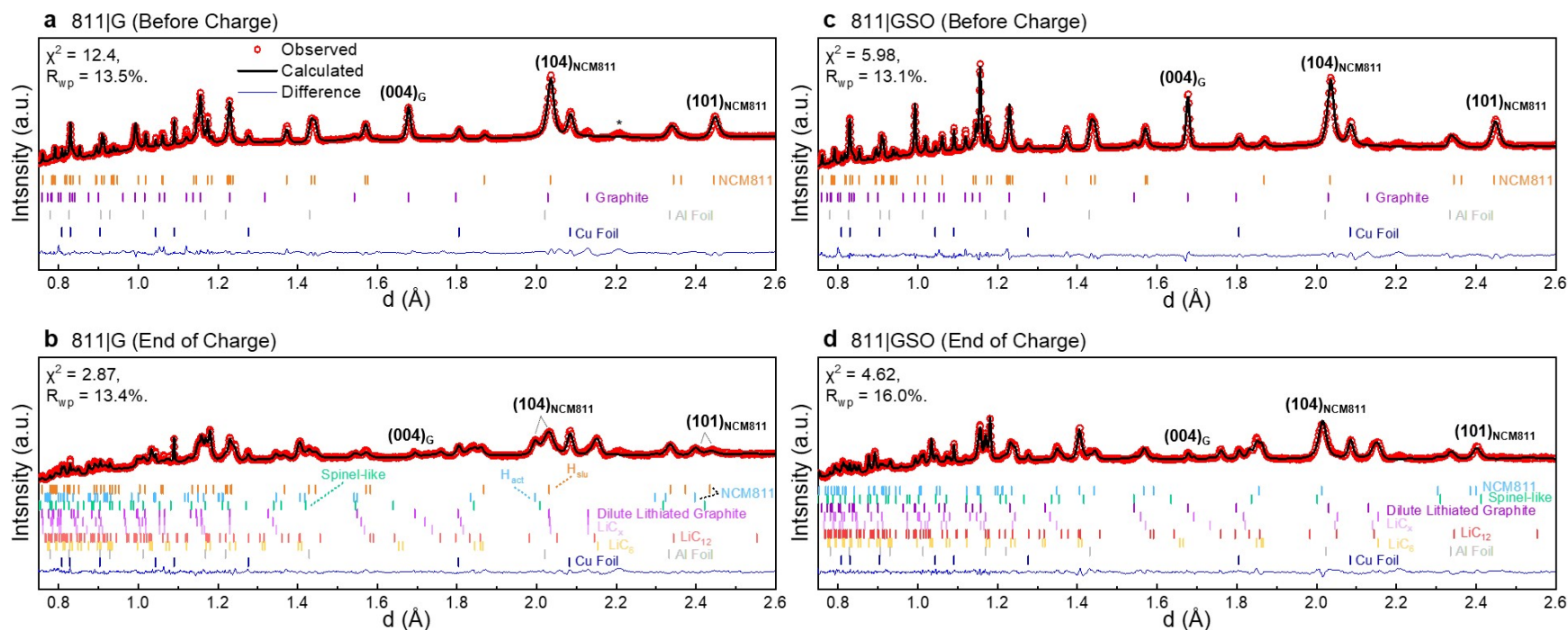
Fig. S8 Rietveld refinements on *operando* neutron diffraction patterns from 0.75 to 2.6 Å of (a) 811|G before charge, (b) 811|G at the end of charge, (c) 811|GSO before charge, and (d) 811|GSO at the end of charge. Bragg reflections of cathode (including the active H_{act}, the sluggish H_{slu}, and the spinel-like part), anode (graphite part only), current collectors are identified on the patterns. Other crystalized but low-contribution components like separators of whom the strongest reflection is marked with "*" in (a), or poor-crystallized components like silicon part of anode are ignored in the refinement. Positions of graphite (004) reflections near 1.7 Å, NCM811 (104) reflections near 2.05 Å, and (101) reflections near 2.45 Å are labelled on the patterns.
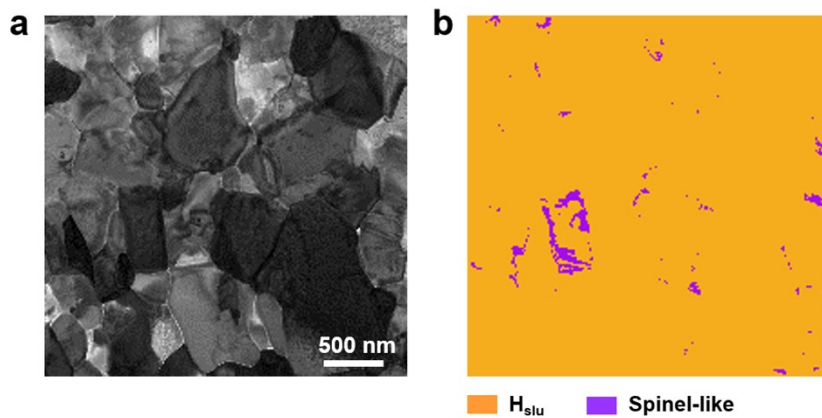
Fig. S9 (a) Virtual ABF image of the pristine NCM811 primary particles before charge. (b) Phase map for cathode particles shown in (a).
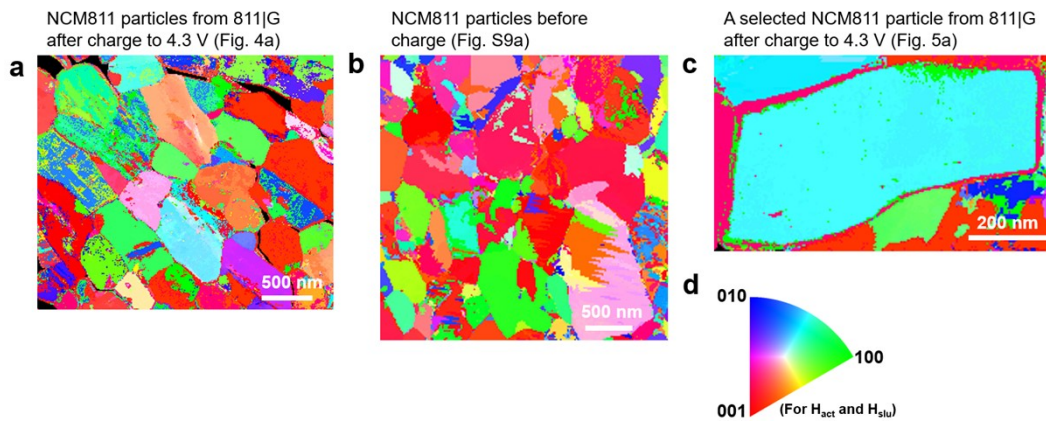
Fig. S10 Crystallographic orientation maps of cathode particles from (a) 811|G after the 1st charge, (b) particles from pristine NCM811 electrodes before charge, and (c) one particle from charged 811|G at the normal direction (ND) of the observation plane, i.e., the direction along incident electron beams. (d) inverse polar figures for hexagonal phases.
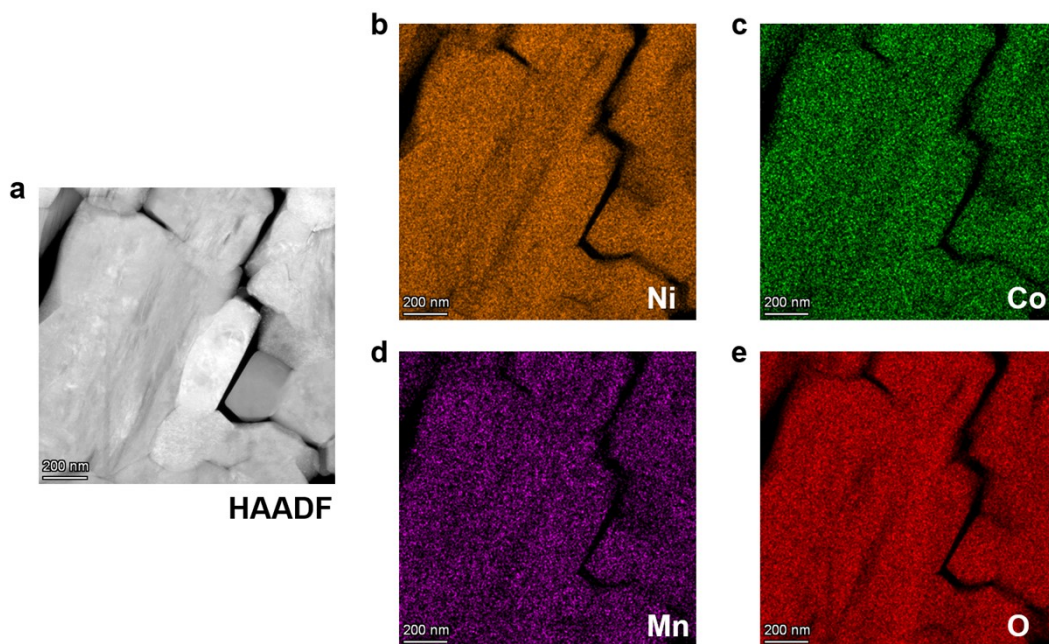
Fig. S11 (a) HAADF image of NCM811 particles from 811|G after charge and the corresponding EDS mappings of elements including (b) nickel, (c) cobalt, (d) manganese, and (e) oxygen, which exhibit uniform distributions at the delithiation state.
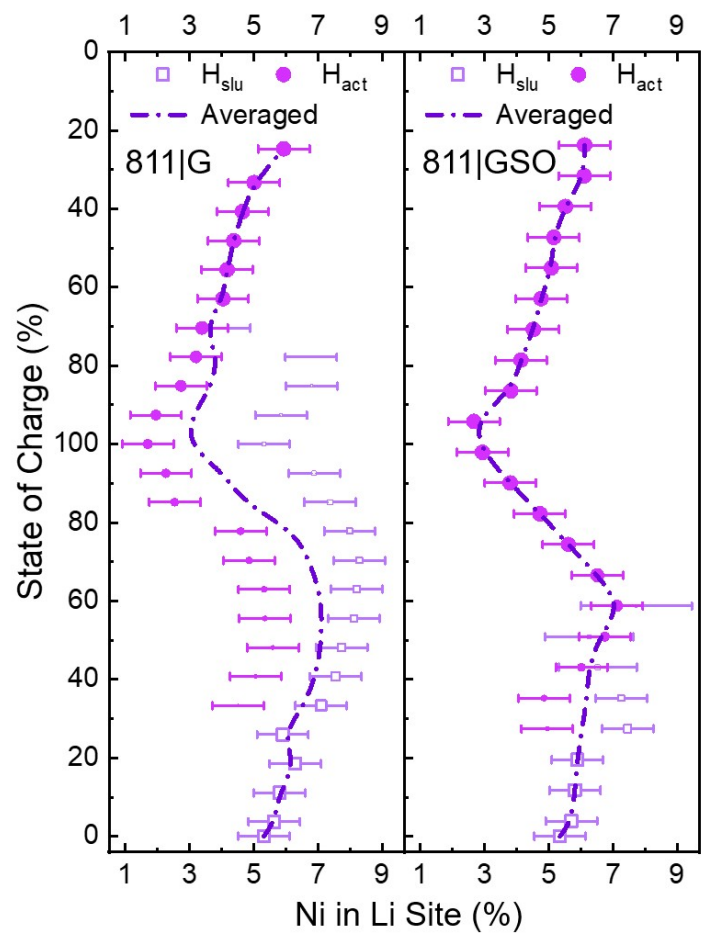
Fig. S12 Evolution of Li/Ni disordering, represented by the occupancy of Ni in Li site (3*a* site), in layered NCM811 cathode from 811|G (left) and 811|GSO (right) during the 1st 0.2C cycling in the *operando* neutron diffraction experiments.
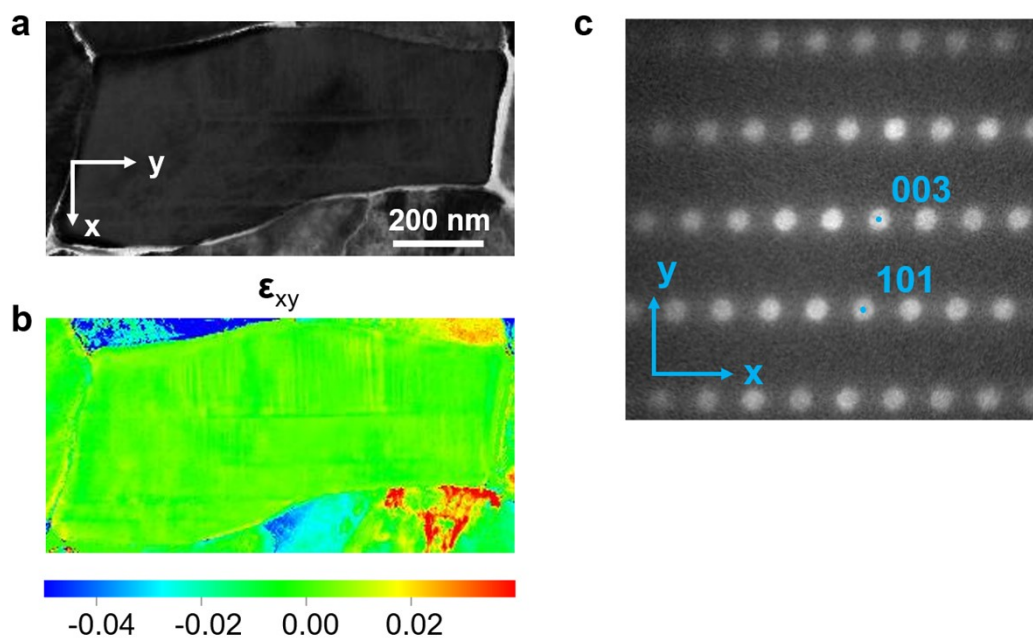
Fig. S13. (a) Virtual ABF image of the charged NCM811 particle with intragranular microcracks in Fig. 5a-d. (b) Distribution of the shear strain ε_{xy} in the selected particle shown in (a). (c) Corresponding summed diffraction pattern.
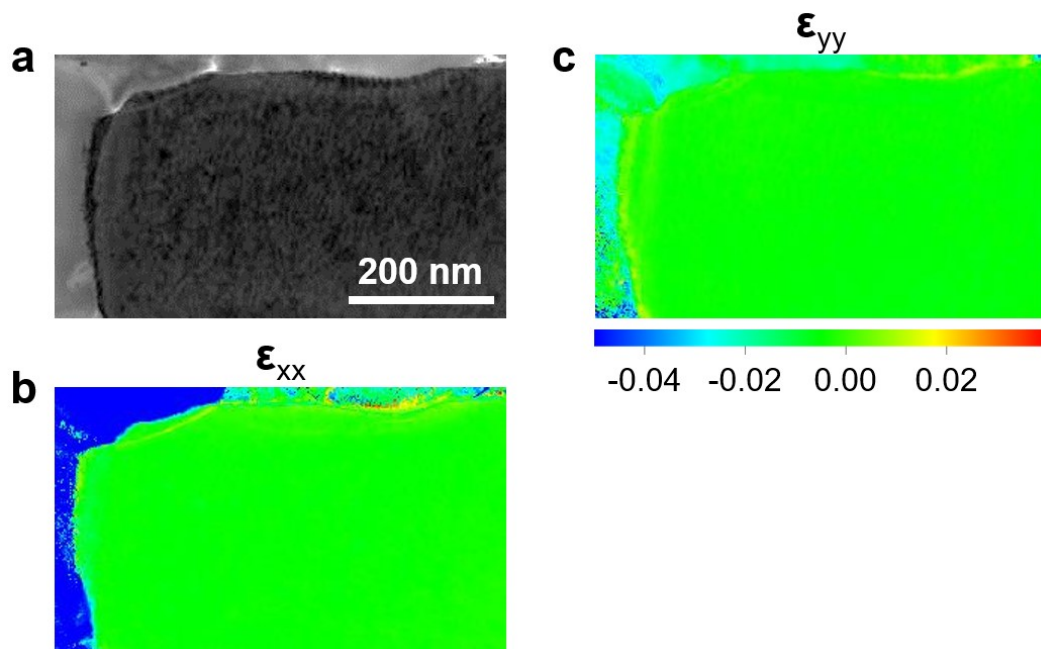
Fig. S14 (a) Virtual ABF image of a pristine NCM811 particle before charge and strain distribution maps of the selected particle shown in (a), including the normal strain in (b) x-direction, ε_{xx}, and (c) y-direction, ε_{yy}.

Table S1 Structure models and the initial parameter values for Rietveld refinements of the phases in full cells

Atom	Wyck. Position	x/a	y/b	z/c	B_{iso} (Å²)	*Occ.*
NCM811 (Layered Structure)						(Cathode)
S.G. $R\bar{3}m$			$a = b = \textbf{2.8716(1)}$ Å[a], $c = \textbf{14.2033(5)}$ Å, $\alpha = \beta = 90°$, $\gamma = 120°$.			
Li	3*a*	0	0	0	1.00	**1-0.05(1)**
Ni (Dis.)	3*a*	0	0	0	1.00	**0.05(1)**
Li (Dis.)	3*b*	0	0	1/2	0.20	**0.05(1)**
Ni	3*b*	0	0	1/2	0.20	0.8-**0.05(1)**
Co	3*b*	0	0	1/2	0.20	0.1
Mn	3*b*	0	0	1/2	0.20	0.1
O	6*c*	0	0	**0.24074(1)**	0.71	1
Spinel-like structure due to over-delithiation[b]						(Cathode)
S.G. $Fd\bar{3}m$ (Origin choice 2)			$a = b = c = \textbf{8.0169(1)}$ Å, $\alpha = \beta = \gamma = 90°$.			
Li (Tet.)	8*a*	1/8	1/8	1/8	1.00	1
Ni (Oct.)	16*d*	1/2	1/2	1/2	0.20	0.8
Co (Oct.)	16*d*	1/2	1/2	1/2	0.20	0.1
Mn (Oct.)	16*d*	1/2	1/2	1/2	0.20	0.1
O	32*e*	0.26523(1)	0.26523(1)	0.26523(1)	0.18	1
2H-Graphite						(Anode)
S.G. $P6_3/mmc$			$a = b = \textbf{2.4604(1)}$ Å, $c = \textbf{6.7200(3)}$ Å, $\alpha = \beta = 90°$, $\gamma = 120°$.			

C (1)	2a	0	0	0	1.50	1
C (2)	4f	1/3	2/3	0.01260(1)	1.50	1

LiC$_{12}$ (Anode)

S.G. P6/mmm $\;\;\;\;\;\;\;\;\;\;\;\;\;\;\;\;$ **a = b = 4.2957(1) Å, c = 7.0417(2) Å, $\alpha = \beta = 90°$, $\gamma = 120°$.**

Li	1a	0	0	0	1.50	1
C	12n	1/3	0	0.25000	1.50	1

LiC$_6$ (Anode)

S.G. P6/mmm $\;\;\;\;\;\;\;\;\;\;\;\;\;\;\;\;$ **a = b = 4.3118(1) Å, c = 3.6946(1) Å, $\alpha = \beta = 90°$, $\gamma = 120°$.**

Li	1a	0	0	0	1.50	1
C	6k	1/3	0	1/2	1.50	1

FCC-Al (Current Collectors)

S.G. Fm$\bar{3}$m $\;\;\;\;\;\;\;\;\;\;\;\;\;\;\;\;$ **a = b = c = 4.0486(1) Å, $\alpha = \beta = \gamma = 90°$.**

Al	4a	0	0	0	0.80	1

FCC-Cu (Current Collectors)

S.G. Fm$\bar{3}$m $\;\;\;\;\;\;\;\;\;\;\;\;\;\;\;\;$ **a = b = c = 3.6144(1) Å, $\alpha = \beta = \gamma = 90°$.**

Cu	4a	0	0	0	0.80	1

[a] **Bold parameters** in the table were allowed to vary during refinements;

[b] Minor spinel-like phase was observed in 4D-STEM for high-voltage NCM811. Therefore, spinel-like structure model was taken into consideration only for patterns collected at the end of charge.

Table S2 Refined cathode structural parameters and anode phase compositions of the 811|G cell under different SOC during the *operando* neutron diffraction experiment

SOC (%)	Layered NCM811 Cathode State [a]								Graphite Anode State			
	Phase	Stoichiometry of Li [b]	Ni in Li Site (%)	a (Å)	c (Å)	c/a	V (Å^3)	C [c]	LiC$_x$ [d]	LiC$_{12}$	LiC$_6$
					- Static -							
0	H$_{slu}$	1	5.3(8)	2.872(6)	14.20(3)	4.95(1)	101.4(5)	○[e]			
					- 1st 0.2C charge -							
3.70	H$_{slu}$	0.95(4)	5.6(8)	2.871(6)	14.21(3)	4.95(1)	101.4(5)	○			
11.11	H$_{slu}$	0.89(4)	5.8(8)	2.869(6)	14.22(3)	4.96(1)	101.4(5)	○	○		
18.52	H$_{slu}$	0.85(4)	6.3(8)	2.867(6)	14.23(3)	4.96(1)	101.3(5)	○	○		
25.93	H$_{slu}$	0.77(4)	5.9(8)	2.866(6)	14.24(3)	4.97(1)	101.3(5)	○	○		
33.33	H$_{slu}$	0.71(4)	7.1(8)	2.866(6)	14.25(3)	4.97(1)	101.4(5)	○	○		
	H$_{act}$	0.68(4)	4.5(8)	2.839(6)	14.32(3)	5.04(1)	99.9(4)				
40.74	H$_{slu}$	0.72(4)	7.6(8)	2.867(6)	14.24(3)	4.97(1)	101.3(5)	○	○	○	
	H$_{act}$	0.54(4)	5.1(8)	2.833(6)	14.38(3)	5.08(1)	100.0(4)				
48.15	H$_{slu}$	0.72(4)	7.7(8)	2.868(6)	14.23(3)	4.96(1)	101.3(5)	○	○	○	
	H$_{act}$	0.57(4)	5.6(8)	2.828(6)	14.45(3)	5.11(1)	100.1(4)				
55.56	H$_{slu}$	0.77(4)	8.1(8)	2.868(6)	14.23(3)	4.96(1)	101.4(5)	○	○	○	
	H$_{act}$	0.53(4)	5.4(8)	2.823(6)	14.46(3)	5.12(1)	99.9(4)				
62.96	H$_{slu}$	0.71(4)	8.2(8)	2.867(6)	14.24(3)	4.97(1)	101.3(5)	○	○	○	○

	H_{act}	0.50(4)	5.3(8)	2.821(6)	14.44(3)	5.12(1)	99.5(4)				
70.37	H_{slu}	0.72(4)	8.3(8)	2.865(6)	14.24(3)	4.97(1)	101.2(5)	○	○	○	○
	H_{act}	0.44(4)	4.9(8)	2.817(6)	14.40(3)	5.11(1)	99.0(4)				
77.78	H_{slu}	0.67(4)	8.0(8)	2.862(6)	14.25(3)	4.98(1)	101.1(5)	○	○	○	○
	H_{act}	0.43(4)	4.6(8)	2.812(6)	14.31(3)	5.09(1)	98.0(4)				
85.19	H_{slu}	0.61(4)	7.4(8)	2.862(6)	14.23(3)	4.97(1)	101.0(5)	○	○	○	○
	H_{act}	0.38(4)	2.5(8)	2.814(6)	13.94(3)	4.95(1)	95.6(4)				
92.59	H_{slu}	0.52(4)	6.9(8)	2.861(6)	14.24(3)	4.98(1)	100.9(5)	○	○	○	○
	H_{act}	0.34(4)	2.3(8)	2.814(6)	13.88(3)	4.93(1)	95.2(4)				
~100	H_{slu}	0.49(4)	5.3(8)	2.861(6)	14.24(3)	4.98(1)	101.0(5)	○	○	○	○
	H_{act}	0.27(4)	1.7(8)	2.813(6)	13.88(3)	4.93(1)	95.2(4)				

- -

- 1st 0.2C Discharge -

- -

92.59	H_{slu}	0.46(4)	5.9(8)	2.860(6)	14.26(3)	4.99(1)	101.0(5)	○	○	○	○
	H_{act}	0.32(4)	2.0(8)	2.814(6)	13.95(3)	4.96(1)	95.7(4)				
85.19	H_{slu}	0.45(4)	6.8(8)	2.860(6)	14.27(3)	4.99(1)	101.1(5)	○	○	○	○
	H_{act}	0.44(4)	2.7(8)	2.818(6)	14.41(3)	5.11(1)	99.1(4)				
77.78	H_{slu}	0.45(4)	6.8(8)	2.861(6)	14.29(3)	4.99(1)	101.3(5)	○	○	○	○
	H_{act}	0.46(4)	3.2(8)	2.822(6)	14.46(3)	5.12(1)	99.7(4)				
70.37	H_{slu}	0.53(4)	4.1(8)	2.859(6)	14.31(3)	5.00(1)	101.3(5)	○	○	○	○
	H_{act}	0.49(4)	3.4(8)	2.824(6)	14.45(3)	5.12(1)	99.8(4)				

62.96	H$_{slu}$	—(f)	—	2.859(6)	14.31(3)	5.00(1)	101.3(5)	○	○	○	○
	H$_{act}$	0.60(4)	4.0(8)	2.835(6)	14.43(3)	5.09(1)	100.4(4)				
55.56	H$_{slu}$	—	—	2.848(6)	14.34(3)	5.04(1)	100.7(5)		○	○	○
	H$_{act}$	0.64(4)	4.2(8)	2.840(6)	14.39(3)	5.07(1)	100.6(4)				
48.15	H$_{act}$	0.68(4)	4.4(8)	2.847(6)	14.35(3)	5.04(1)	100.7(5)		○	○	
40.74	H$_{act}$	0.73(4)	4.7(8)	2.852(6)	14.32(3)	5.02(1)	100.8(5)		○	○	
33.33	H$_{act}$	0.77(4)	5.0(8)	2.856(6)	14.29(3)	5.00(1)	100.9(5)	○	○	○	
24.73	H$_{act}$	0.85(4)	5.9(8)	2.861(6)	14.27(3)	4.99(1)	101.2(5)	○	○	○	
End	H$_{act}$	0.86(4)	6.4(8)	2.863(6)	14.26(3)	4.98(1)	101.2(5)	○	○	○	

[a] Information of the slight spinel-like phase observed at high SOC is not included;

[b] Total ratio of Li occupancy at 3a (Li site) and 3b (Ni site) sites. Assume that no Li vacancy existed in the initial structure;

[c] "C" includes pure graphite or dilute lithiated graphite (stage 1L);

[d] "LiC$_x$" includes high-order GICs (stage 2L ~ 4L), e.g., LiC$_{18}$, LiC$_{30}$, LiC$_{40}$, etc.;

[e] ○ - The graphite/GIC phase is observed at this SOC. Blank - The graphite/GIC phase is absent at this SOC;

[f] Due to the low remaining amount of H$_{slu}$, it is difficult to acquire reliable results of the parameters. (Also applicable to **Table S3**)

Table S3 Refined cathode structural parameters and anode phase compositions of the 811|GSO cell under different SOC during the operando neutron diffraction experiment

SOC (%)	Layered NCM811 Cathode State							Graphite Anode State			
	Phase	Stoichiometry of Li	Ni in Li Site (%)	a (Å)	c (Å)	c/a	V (Å³)	C	LiC_x	LiC_{12}	LiC_6
- Static -											
0	H_{slu}	1	5.4(8)	2.872(6)	14.20(3)	4.94(1)	101.4(5)	○			
- 1st 0.2C Charge -											
3.92	H_{slu}	0.98(4)	5.7(8)	2.870(6)	14.20(3)	4.95(1)	101.3(5)	○			
11.75	H_{slu}	0.97(4)	5.8(8)	2.870(6)	14.22(3)	4.96(1)	101.4(5)	○	○		
19.58	H_{slu}	0.92(4)	5.9(8)	2.865(6)	14.23(3)	4.97(1)	101.2(5)	○	○	○	
27.41	H_{slu}	1.00(4)	7.5(8)	2.868(6)	14.22(3)	4.96(1)	101.3(5)	○	○	○	
	H_{act}	0.84(4)	5.0(8)	2.845(6)	14.35(3)	5.04(1)	100.6(4)				
35.25	H_{slu}	0.95(4)	7.3(8)	2.867(6)	14.23(3)	4.96(1)	101.3(5)	○	○	○	
	H_{act}	0.83(4)	4.9(8)	2.841(6)	14.37(3)	5.06(1)	100.4(4)				
43.08	H_{slu}	0.85(8)	6.5(1.2)	2.869(6)	14.24(3)	4.96(1)	101.5(5)	○	○	○	
	H_{act}	0.81(4)	6.0(8)	2.839(6)	14.41(3)	5.08(1)	100.5(4)				
50.91	H_{slu}	0.78(9)	6.3(1.4)	2.871(6)	14.25(3)	4.96(1)	101.7(5)	○	○	○	○
	H_{act}	0.80(4)	6.8(8)	2.836(6)	14.44(3)	5.09(1)	100.6(4)				
58.75	H_{slu}	0.86(11)	7.7(1.7)	2.873(6)	14.22(3)	4.95(1)	101.7(5)	○	○	○	○
	H_{act}	0.77(4)	7.1(8)	2.831(6)	14.47(3)	5.11(1)	100.5(4)				

66.58	H_{slu}	—	—	2.873(6)	14.23(3)	4.95(1)	101.7(5)	○	○	○	○
	H_{act}	0.71(4)	6.5(8)	2.828(6)	14.48(3)	5.12(1)	100.3(4)				
74.41	H_{slu}	—	—	2.874(6)	14.23(3)	4.95(1)	101.8(5)	○	○	○	○
	H_{act}	0.64(4)	5.6(8)	2.824(6)	14.48(3)	5.13(1)	100.0(4)				
82.24	H_{act}	0.56(4)	4.7(8)	2.820(6)	14.47(3)	5.13(1)	99.7(4)	○	○	○	○
90.08	H_{act}	0.48(4)	3.8(8)	2.817(6)	14.42(3)	5.12(1)	99.1(4)	○	○	○	○
97.91	H_{act}	0.36(4)	2.9(8)	2.812(6)	14.30(3)	5.08(1)	98.0(4)	○	○	○	○

- 1st 0.2C Discharge -

94.26	H_{act}	0.39(4)	2.7(8)	2.814(6)	14.36(3)	5.10(1)	98.4(4)	○	○	○	○
86.42	H_{act}	0.45(4)	3.8(8)	2.819(6)	14.45(3)	5.12(1)	99.4(4)	○	○	○	○
78.59	H_{act}	0.51(4)	4.1(8)	2.822(6)	14.49(3)	5.13(1)	99.9(4)	○	○	○	○
70.76	H_{act}	0.58(4)	4.5(8)	2.825(6)	14.49(3)	5.13(1)	100.2(4)	○	○	○	○
62.93	H_{act}	0.64(4)	4.8(8)	2.830(6)	14.46(3)	5.11(1)	100.3(4)	○	○	○	○
55.09	H_{act}	0.70(4)	5.1(8)	2.837(6)	14.42(3)	5.08(1)	100.5(4)	○	○	○	
47.26	H_{act}	0.78(4)	5.2(8)	2.842(6)	14.38(3)	5.06(1)	100.6(4)	○	○	○	
39.43	H_{act}	0.79(4)	5.5(8)	2.849(6)	14.34(3)	5.03(1)	100.9(5)	○	○		
31.59	H_{act}	0.81(4)	6.1(8)	2.855(6)	14.31(3)	5.01(1)	101.0(5)	○	○		
23.76	H_{act}	0.84(4)	6.1(8)	2.860(6)	14.28(3)	4.99(1)	101.1(5)	○	○		
End	H_{act}	0.87(4)	5.9(8)	2.862(6)	14.25(3)	4.98(1)	101.1(5)	○			

Table S4 Qualitative size and phase distribution of marked primary particles from the 4D-STEM large-area scanning result

No.	Size	Phase Distribution		
		H_{act}	H_{slu}	Spinel-like
1	Medium	Main	Minor near surface, little in the bulk	Little near surface
2	Large	Main	Minor	Little
3	Medium	Main	Minor near surface, little in the bulk	Minor near surface, little in the bulk
4	Medium	Main	Minor	Minor near surface
5	Small	Almost not observed	Main	Almost not observed
6	Large	Main	Minor in the bulk	Almost not observed
7	Small	Main	Little	Little
8	Large	Minor	Little	Main
9	Medium	Main	Minor near surface, little in the bulk	Almost not observed
10	Large	Minor	Main	Almost not observed
11	Small	Main	Minor near surface, little in the bulk	Almost not observed
12	Large	Main	Minor near surface, little in the bulk	Little
13	Medium	Minor	Little	Main
14	Medium	Little in the bulk	Main	Little in the bulk
15	Large	Minor	Main	Almost not observed
16	Small	Main	Minor near surface, little in the bulk	Almost not observed
17	Medium	Main	Minor near surface, little in the bulk	Almost not observed

18	Large	Minor	Main	Almost not observed
19	Large	Main	Minor near surface, little in the bulk	Little near surface
20	Medium	Main	Little	Minor near surface, little in the bulk

References

1. Z. Huang, M. Chu, R. Wang, W. Zhu, W. Zhao, C. Wang, Y. Zhang, L. He, J. Chen, S. Deng, L. Mei, W. H. Kan, M. Avdeev, F. Pan and Y. Xiao, *Nano Energy*, 2020, **78**, 105194.

2. W. Wu, M. Wang, J. Wang, C. Wang and Y. Deng, *ACS Appl. Energy Mater.*, 2020, **3**, 3884-3892.

3. W. Wu, M. Wang, R. Wang, D. Xu, H. Zeng, C. Wang, Y. Cao and Y. Deng, *J. Power Sources*, 2018, **407**, 112-122.

4. J. Chen, L. Kang, H. Lu, P. Luo, F. Wang and L. He, *Physica B Condens. Matter*, 2018, **551**, 370-372.

5. J. Rodríguez-Carvajal, *Physica B Condens. Matter*, 1993, **192**, 55-69.

6. C. Wang, R. Wang, Z. Huang, M. Chu, W. Ji, Z. Chen, T. Zhang, J. Zhai, H. Lu, S. Deng, J. Chen, L. He, T. Liang, F. Wang, J. Wang, Y. Deng, W. Cai and Y. Xiao, *Energy Stor. Mater.*, 2022, **44**, 1-9.

7. Y. Xiao, T. Liu, J. Liu, L. He, J. Chen, J. Zhang, P. Luo, H. Lu, R. Wang, W. Zhu, Z. Hu, G. Teng, C. Xin, J. Zheng, T. Liang, F. Wang, Y. Chen, Q. Huang, F. Pan and H. Chen, *Nano Energy*, 2018, **49**, 77-85.

8. K. Momma and F. Izumi, *J. Appl. Crystallogr.*, 2011, **44**, 1272-1276.